energies

Article

Effect of Circumferential Single Casing Groove Location on the Flow Stability under Tip-Clearance Effect in a Transonic Axial Flow Compressor Rotor

Xiaoxiong Wu, Bo Liu, Botao Zhang and Xiaochen Mao *

School of Power and Energy, Northwestern Polytechnical University, Xi'an 710129, China; wxx1990@mail.nwpu.edu.cn (X.W.); liubo704npu@126.com (B.L.); zhangbotao@mail.nwpu.edu.cn (B.Z.)
* Correspondence: maoxiao_chen@nwpu.edu.cn

Abstract: Numerical simulations have been performed to study the effect of the circumferential single-grooved casing treatment (CT) at multiple locations on the tip-flow stability and the corresponding control mechanism at three tip-clearance-size (TCS) schemes in a transonic axial flow compressor rotor. The results show that the CT is more efficient when its groove is located from 10% to 40% tip axial chord, and G2 (located at near 20% tip axial chord) is the best CT scheme in terms of stall-margin improvement for the three TCS schemes. For effective CTs, the tip-leakage-flow (TLF) intensity, entropy generation and tip-flow blockage are reduced, which makes the interface between TLF and mainstream move downstream. A quantitative analysis of the relative inlet flow angle indicates that the reduction of flow incidence angle is not necessary to improve the flow stability for this transonic rotor. The control mechanism may be different for different TCS schemes due to the distinction of the stall inception process. For a better application of CT, the blade tip profile should be further modified by using an optimization method to adjust the shock position and strength during the design of a more efficient CT.

Keywords: transonic axial flow compressor; grooved casing treatment; tip-leakage flow; stall margin; flow stability

Citation: Wu, X.; Liu, B.; Zhang, B.; Mao, X. Effect of Circumferential Single Casing Groove Location on the Flow Stability under Tip-Clearance Effect in a Transonic Axial Flow Compressor Rotor. *Energies* **2021**, *14*, 6143. https://doi.org/10.3390/en14196143

Received: 1 September 2021
Accepted: 24 September 2021
Published: 27 September 2021

1. Introduction

It has long been known that rotor tip-leakage flow (TLF) has a significant influence on the compressor overall performance in terms of efficiency, pressure rise capability and safe operating range [1,2]. Generally, TLF often exists in the tip region in a form of tip-leakage vortex (TLV). In transonic compressors, the tip flow is further complicated due to the interaction between the passage shock wave, secondary flow and TLF/TLV. In the past several decades, considerable research has been performed to gain a deep understanding of the flow mechanisms of TLF and the tip-clearance effect [3–5].

TLF is an important factor leading to flow instability such as compressor rotating stall [6,7]. At present, the main explanations for this phenomenon are TLV breakdown and self-excited vibration. The former states that the vortex breakdown is the root cause of passage blockage and unsteady flow near the blade tip [8,9]. The latter holds that the real reason for the occurrence of stall inception is the inherent dynamic balance between the blade force and the loss force caused by the TLF [10–12], while there is no absolute association with the TLV breakdown. However, both show that TLF affects the stable operation of the compressor. Effectively improving the quality of the blade tip-flow field is one of the important ways to improve the compressor stall margin. Compared to axial compressor, TLF also plays a key role in the flow stability of the centrifugal compressor. Grondin et al. [13] found that the TLF due to the high-pressure gradient convects to the front of adjacent blade and the triggers rotating stall of an unshrouded centrifugal compressor. Besides, the diffuser vanes influenced the stall cells of a transonic centrifugal compressor by boundary layer separation on the suction side in a study by Trébinjac et al. [14]. Cravero et al. [15,16] developed models to identify the instability operating range based on an analysis of different flow structures at low and high rotational speeds, respectively, which is promising for the design of centrifugal compressors.

As an effective approach to reduce the detrimental effect of aerodynamic instabilities, casing treatment (CT) is often used to improve the flow stability in the compression system of aircraft engines. The development of a range of different CTs in compressors was best depicted by Hathaway [17]. Additionally, compared with slot-based CT, a grooved CT can offer better mechanical integrity with less impact on the compressor efficiency [18]. To make the groove design better, numerous studies have been carried out to uncover the corresponding mechanism of flow stability enhancement by grooved CT [19–21]. The results have indicated that rotor TLF contributes a lot to the stall inception process and the compressor stall margin improvement (SMI) strongly correlates with the interaction between casing groove and rotor tip flow.

The investigation into the CT effect and its corresponding contribution to the SMI with a single groove is an effective way to reveal the flow control mechanism of grooved CT. Several investigations have been conducted to explore the effectiveness of a single groove CT at different locations to improve the compressor flow stability in subsonic compressors [22–27]. The application of circumferential grooved CT in a low-speed axial compressor was studied experimentally by Liu et al. [26]. The results show that the single circumferential slot could significantly improve the stall margin, but the type of stall inception was not changed. For the transonic compressor, whose flow field is more complex due to the existence of shock wave, Sakuma et al. [28,29] and Mirzabozorg et al. [30] have numerically investigated the effect of circumferential single-grooved CTs on the stability enhancement. However, there still exists disagreement in the literature about how the grooves work effectively and where they should be located due to the stall inception process and the fact that the groove working principles are not fully understood. Therefore, more research efforts should be spent to study the effect of CT with a single groove at different axial locations on the SMI and corresponding mechanism.

With the design of modern axial compressors trending toward higher pressure ratio, the rotor relative tip clearance becomes larger due to the lower annulus height and smaller blades in the compressor later stages. Additionally, transient operations and thermal expansion can also lead to a change of rotor tip clearance. At present, casing treatments based on circumferential grooves are also being investigated to eliminate or relieve the negative effect associated with an increase of rotor tip clearance. The impact of circumferential groove CT on the performance of low-speed compressors with different tip clearances has been studied by Takata and Tsukuda [18,31]. The results indicated that the grooves were most effective at a small-tip clearance. Rolfes et al. [32,33] experimentally found that the increment of normal operating range benefited from the circumferential groove CT at the small-tip clearance is negligible for a low-speed axial flow compressor; however, both the compressor stall margin and efficiency were improved for the large-tip clearance case. With the help of simulations, Hamzezade et al. [34] also found that a circumferential groove CT placed near the trailing edge of the first stage rotor is more efficient for a larger tip gap size in a multistage axial compressor. A numerical parametric study of tip clearance coupled with circumferential groove CT for a transonic axial flow compressor was numerically investigated by Beheshti et al. [35]. They also found that the circumferential groove CTs are more efficient with a large tip gap. Cevik et al. [36] numerically found that a proper designed circumferential groove CT is able to mitigate the sensitivity of performance and stall margin-to-tip clearance in a high-speed subsonic axial flow compressor. A similar conclusion was also observed by Fujita and Takata [18] in a low-speed compressor. However, there is still a lack of relevant research of an impact of single-grooved CT location on the tip-flow stability with considering tip-clearance effect in a transonic compressor rotor.

Therefore, the present work will investigate the effect of single-grooved CT at different locations on the tip-flow stability under the influence of tip clearance of a transonic compressor rotor. The focus of the current paper mainly includes two aspects. First, a parametric study was performed concerning the axial location of a single casing groove in terms of SMI at three different tip clearances. Second, the variation of tip flow behaviors and the corresponding control mechanisms were analyzed for the result of the parametric study. The organization of this paper consists of five sections. The compressor rotor is briefly introduced in Section 2 following the CT design scheme. The numerical approach is described and validated in Section 3. The parametric study is conducted, and the results are analyzed in Section 4. At last, the conclusions are summarized in Section 5.

2. Investigated Compressor Rotor and Design of Grooved CTs

2.1. Description of the Target Transonic Compressor Rotor

The test case studied in this paper is a high-speed axial compressor rotor of the NASA Stage35 [37]. Figure 1 shows the cross-sectional diagram of the transonic compressor stage. The detailed design parameters of the rotor are listed in Table 1.

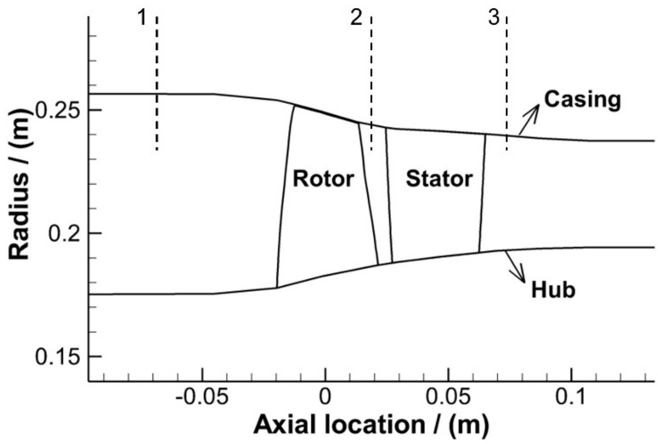

Figure 1. Schematic diagram of the transonic compressor stage.

Table 1. Main design parameters of the transonic rotor.

Design Parameters	Values
Rotational speed	17,188.7 r/min
Mass-flow rate	20.2 kg/s
Pressure ratio	1.8
Number of blades	36
Aspect ratio	1.19
Inlet-tip diameter	0.504 m
Relative tip speed	454.5 m/s
Tip clearance	0.408 mm

It's necessary to consider the influence of the stator when studying the whole compressor; however, the stator is not included here for following reasons. First, this compressor was designed as an inlet stage and there is no inlet guide vane in the test rig. To maintain consistency with the experimental conditions, no upstream stator is introduced. Second, according to the public research, the leakage flow at the rotor tip clearance mainly contributes to the stall of this compressor compared to the flow in the stator row. It has lower consumption of computation resource to exclude the stator row. Additionally, Chen et al. [38] have studied the prestall behavior of the NASA compressor stage 35 with full-annulus grid model via time-accurate numerical simulation method. It is found that the initiation of the spike inception occurred in the rotor tip region, and it is closely related to the rotor tip-leakage flow. Accordingly, it can be considered reasonable to research the rotor alone.

2.2. Design of Circumferential Grooved CTs

In the current paper, eleven circumferential single grooves on the shroud of rotor were studied for each of the three different tip-clearance-size (TCS) schemes. The three different TCS schemes are τ, 1.5τ and 2τ (τ corresponds to the design TCS). Therefore, a total of thirty-three casing groove schemes were investigated. Figure 2 shows the structure of the circumferential groove CT and enlarged details. As shown in the upper-right corner of Figure 2, the length between the leading edges of blade and the grove is normalized by the tip axial chord as dimensionless axial location of the grove. The axial depth and width of all the grooves are 4 mm and 2 mm, giving an aspect ratio (*AR*) of 2, which is the same as that in Refs. [23–25]. The H-type grids of the single groove generated by IGG [39] has 0.65×10^5 nodes with 21 axial, 45 radial and 69 tangential points. The full non-matching connecting technology was used to connect the mesh of a casing groove and the main blade passage.

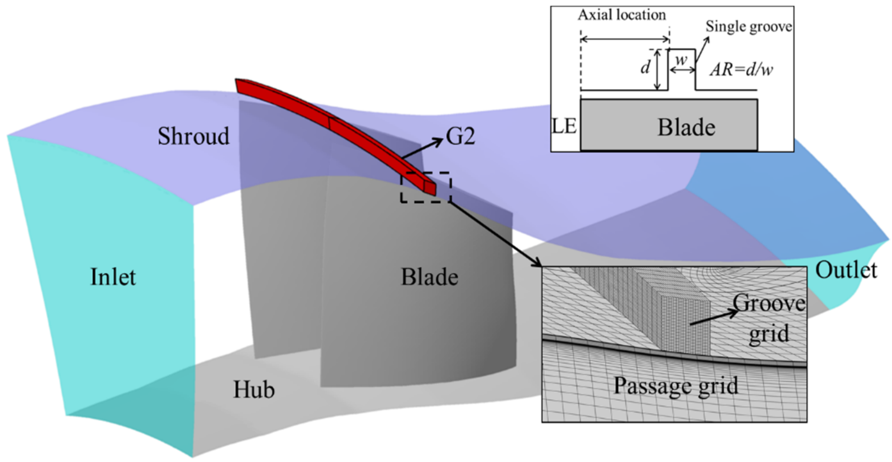

Figure 2. Schematic of a circumferential grooved CT and the details of the groove.

3. Numerical Approach and Validation

The commercial RANS solver FINE/TURBO [40] was used for the numerical simulations in this paper. Single-passage steady simulations were performed by using the periodical boundary conditions on the two sides. The equation uses the explicit four-order Runge-Kutta method to discretize time and uses the cell-central finite volume scheme to discretize space. Since the Spallart–Almaras turbulence model [41] has good convergence and has been widely used in the numerical simulation of turbomachinery [42,43], the internal turbulence flow was predicted by the Spallart–Almaras modal to save the computing resource.

The O4H-type mesh of blade passage was created by AUTOGRID5 [44]. The real rotor tip gap was modeled by the butterfly topology [45]. To ensure the accuracy of numerical predictions, Figure 3 shows the variation of the overall aerodynamic performance parameters of the compressor with the number of grids under the conditions of near-design point and near-stall point. When the number of grids exceeds 1 million, the pressure ratio and efficiency tend to be stable, and the influence of grids on the numerical results can be ignored. Considering computational accuracy and cost, the total grid number of 1.03×10^6 is selected for the blade passage, and the grid setup for the blade passage is similar to that in Ref. [39] in spanwise, streamwise and tangential directions. There are 17 nodes for the design rotor tip gap, and the number of grid node was increased for the larger tip clearances. The grid is gradually densified close to the end wall until the thickness of the first layer near the wall reaches 5×10^{-6} m to ensure that y+ is less than 3 (refer to Figure 4). The grid of one blade passage is shown in Figure 5 as well as the detailed mesh topology of leading edge (LE) and trailing edge (TE).

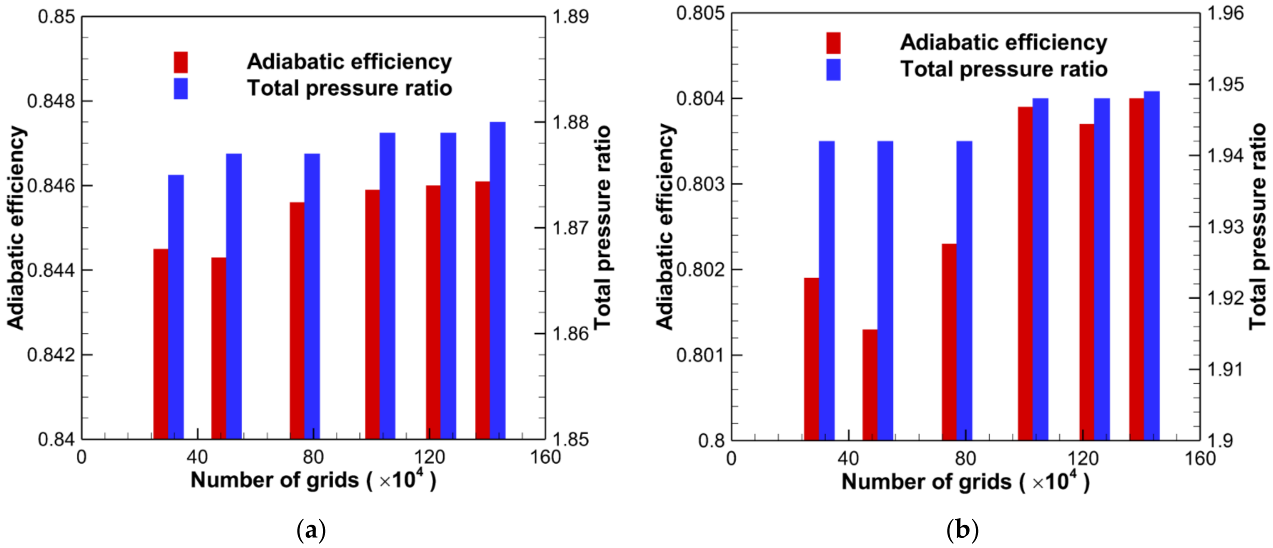

Figure 3. Variation of the overall aerodynamic performance parameters of the compressor with the number of grids: (**a**) peak efficiency point; (**b**) nNear-stall point.

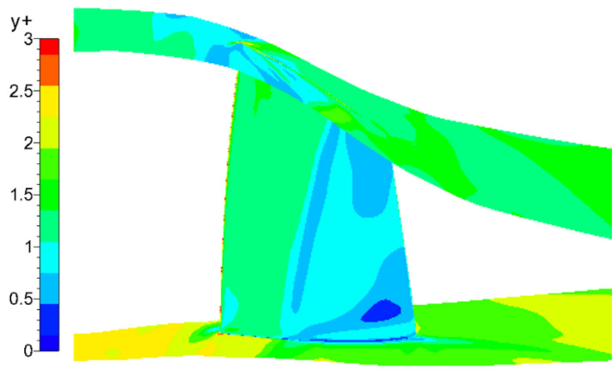

Figure 4. The y plus on the solid wall.

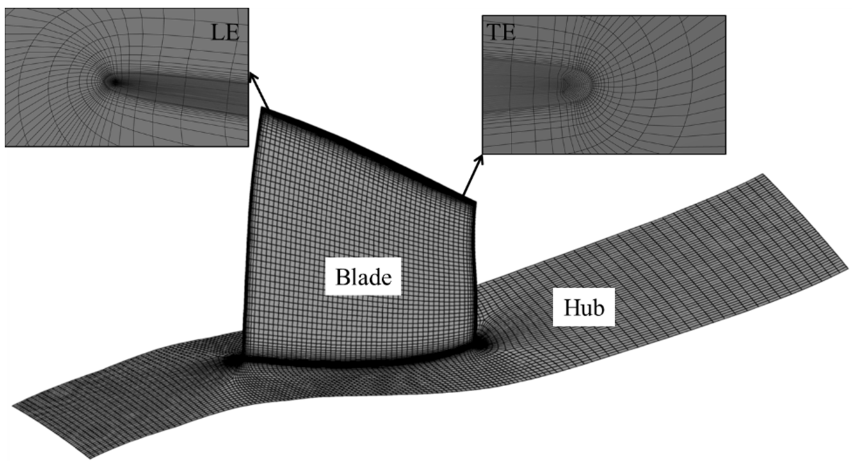

Figure 5. The computational mesh of the compressor rotor.

In the computations, the parameters of inlet flow angles, total temperature and total pressure were specified as the inlet boundary conditions. The turbulent viscosity at the inlet was set to 0.0001 m^2/s. The mid-span static pressure based on radial equilibrium law was given as outlet boundary condition. The solid walls were set to be adiabatic and non-slip.

To validate the numerical approach used in this work, a comparison between the predicted overall performance and the experimentally measured value at the design speed is plotted in Figure 6. The relative errors of calculation at near-stall point (NSP) and near-design point (NDP) are listed in Table 2. In the calculation process, the mass flow gradually moves to the stall boundary as the outlet pressure increases until reaches the stability limit. The dichotomy is used to adjust the pressure to ensure that the stall margin is accurately obtained. [46]. From Figure 6 and Table 2, the relative overall error of the adiabatic efficiency is within 1.85%, and the maximum error of the total pressure ratio is no more than 4.7%. Although there is a discrepancy (about 1.6%) for the mass-flow rate at the choke condition between the numerical and experimental results, the numerical results are consistent with the trend of the experimental data in most work conditions, and the predicted stall point is almost the same as that in the experiment.

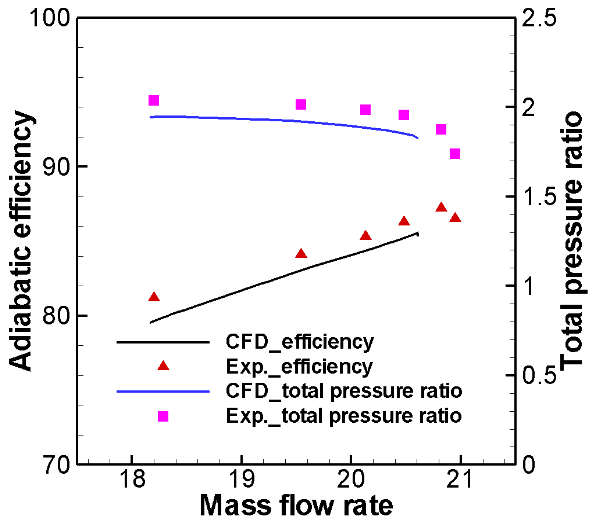

Figure 6. Comparison of the calculated and experimental overall performance.

Table 2. The error of calculation on overall performance.

Parameters	Experiment	Calculation	Calculation Error
Mass flow at NSP (kg/s)	18.2	18.21	0.05%
Total pressure ratio at NSP	2.036	1.945	4.47%
Adiabatic efficiency at NSP	0.812	0.797	1.85%
Mass flow at NDP (kg/s)	20.13	20.05	0.40%
Total pressure ratio at NDP	1.985	1.892	4.69%
Adiabatic efficiency at NDP	0.853	0.842	1.29%

The spanwise distribution of total pressure ratio and total temperature ratio of numerical and experimental results at near-stall work condition (18.21 kg/s) are compared in Figure 7. Both the total pressure ratio and total temperature ratio are pitch-averaged at the Station 2 shown in Figure 1. The predicted values and experimental results match reasonably well with each other, in which the average error is about 2%. Accordingly, the numerical method is reliable enough to be used to estimate the overall characteristics and flow field, so that reliable conclusions about the CT scheme can also be obtained.

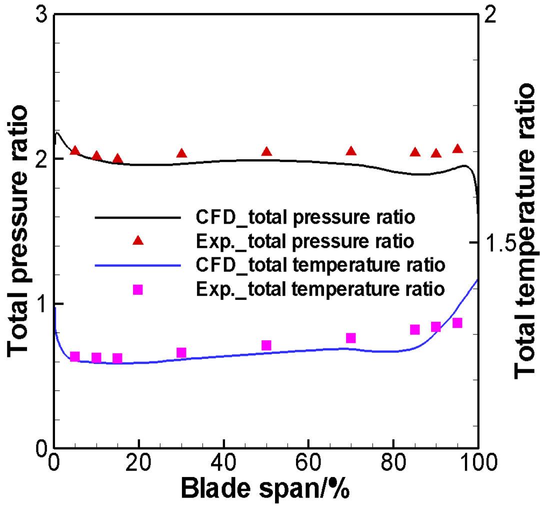

Figure 7. Comparison of pitch-averaged total pressure ratio and total temperature ratio.

4. Results and Discussion

4.1. Effect of CTs on the Stall-Margin Improvement

Parametric study was performed with respect to the axial location of the single casing grooves, and 11 circumferential single grooves were studied for each of the three different TCS schemes (τ, 1.5τ and 2τ). In this work, each CT configuration labeled by GX depends on the axial location of its groove. The symbol GX means the grove located at dimensionless axial location of 0.X on shroud where X is an integer from 0 to 10.

For clarity, only the overall performance of the best CT schemes at two different TCS scheme are presented here. Figure 8 shows the efficiency and total pressure characteristics derived from the computations for the CT scheme of G2 at the tip gaps of τ and 2τ. Compared with the smooth wall (SW) case, the mass-flow rate of stall point is reduced obviously for G2 at both the TCS schemes. It should be mentioned that the efficiency of the CT schemes is increased to a different extent for the two TCS schemes due to the improvement of tip-flow field at the near-stall point of the SW case (NSP1 and NSP2 correspond to the near-stall condition of the SW case at the TCS of τ and 2τ, respectively), especially for the TCS of τ. However, there is almost no efficiency change for the CT schemes at the near-design point (NDP). Additionally, the characteristic lines of total pressure ratios experience similar changes to the adiabatic efficiency.

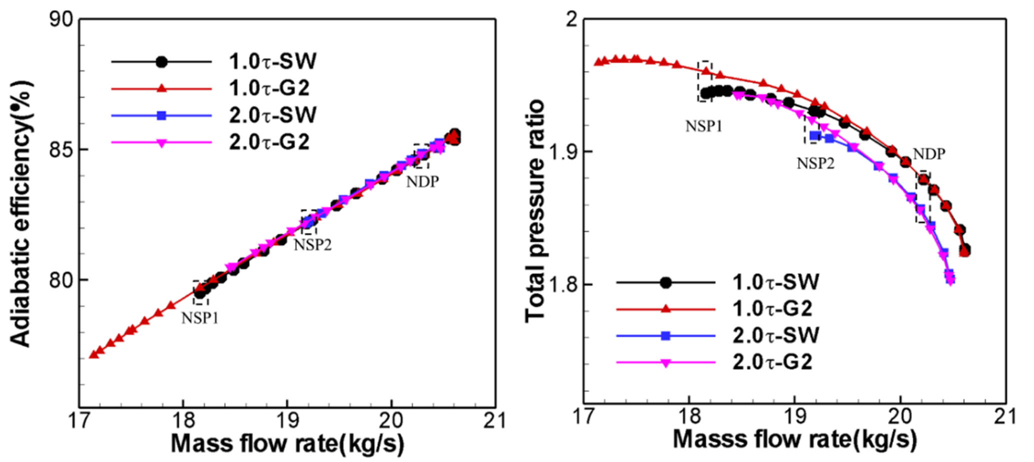

(**a**) (**b**)

Figure 8. Overall characteristics plots for the CT scheme of G2 at two different TCS schemes: (**a**) adiabatic efficiency; (**b**) total pressure ratio.

The stall-margin improvement (SMI) defined as follow is taken to evaluate the effectiveness of the CT schemes:

$$SMI = \left[\frac{\pi_{stall} m_{design}}{\pi_{design} m_{stall}} - 1\right]_{CT} - \left[\frac{\pi_{stall} m_{design}}{\pi_{design} m_{stall}} - 1\right]_{SW} \tag{1}$$

where π and m are the total pressure ratio and mass-flow rate, *stall* and *design* represent the near-stall and near design conditions, and subscripts *CT* and *SW* refer to the cases of smooth wall and casing treatment, respectively.

Figure 9 presents the calculated SMI for each groove configuration at three different TCS schemes. One can see that the CT improves the flow stability more when the grooves are located from 10% to 40% tip axial chord and G2 is the best CT scheme for all the three TCS schemes. The SMI decreases gradually as the groove location is shifted downstream from the position of 20% tip axial chord. The best scheme of G2 improves the stall margin by about 8.3%, 8.2% and 6.2% at the TCS of τ, 1.5τ and 2τ, respectively. Considering the uncertainty of steady single-passage calculations at the stall work condition, the effect of the CTs after 50% tip axial chord and near the leading edge on the SMI seems insignificant. Compared with the TCS of τ, the SMI remains almost unchanged when the casing grooves are located at the position of 10% and 20% tip axial chord at the TCS of 1.5τ, while the SMI is slightly higher for other CT schemes. As the TCS is increased to 2τ, the SMI is reduced obviously before the position of 30% tip axial chord. However, there is no remarkable change of SMI at the position of 30% and 40% tip axial chord. Overall, the CT schemes are most effective at the TCS of 1.5τ.

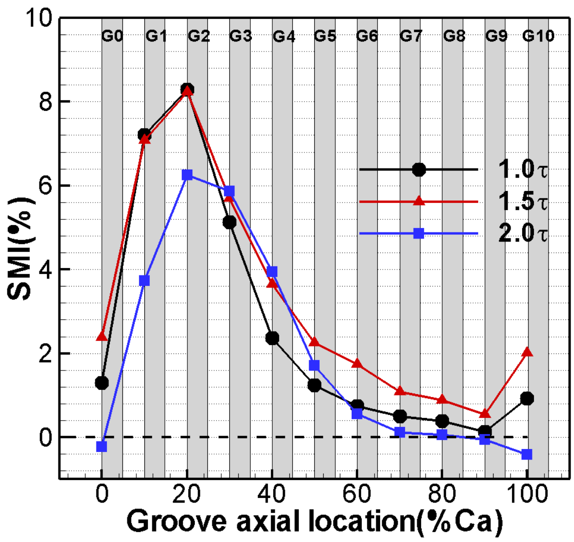

Figure 9. SMI trends as a function of groove location at three different TCS schemes.

The sensitivity results of SMI to tip clearance for the four more efficient CT schemes (G2, G3, G4 and G5) are shown in Figure 10. It can be seen the sensitivity of SMI is lowest for G3 compared with other CT schemes and G4 is another better option. At the TCS of 2τ, the SMI of G3 (5.9%) is only slightly lower than the best CT scheme of G2 (6.2%). Therefore, the CT scheme of G2 is the best choice to improve the flow stability without considering the sensitivity of SMI within a certain range of TCS variation. However, the CT schemes of G3 and G4 may be two better options to reduce the effect of the sensitivity of SMI during the design of CT scheme with multi-grooves based on the CT of G2.

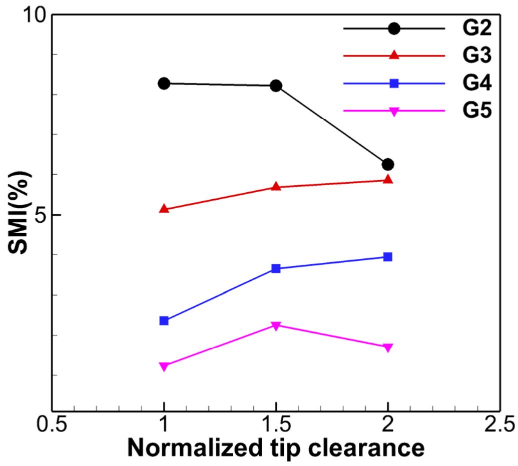

Figure 10. Sensitivity results of SMI for four different CT schemes.

4.2. Effect of CTs on the Tip Flow Behaviors

Since TLF mainly contributes to the stall inception process near the blade tip, the effect of CT on the tip-flow field and the corresponding mechanism will be analyzed at two TCS schemes in this section. The best CT scheme of G2 together with the SW case will be selected to explore the impact of CT at the TCS schemes of τ and 2τ in detail. The analysis was conducted at the near-stall condition (NSP1 for TCS of τ, and NSP2 for TCS of 2τ), which was marked in Figure 8.

Table 3 lists the aerodynamic parameters of the compressor at NSP1 and NSP2 under the TCS of τ and 2τ, respectively, under the prototype smooth casing and casing treatment G2 scheme, and the relative changes after casing treatment are also given. By casing treatment, the total pressure ratio and adiabatic efficiency of the compressor are slightly improved at the same mass flow, indicating that casing treatment is effective for the modification of the flow field. However, as the TCS increases from τ to 2τ, the effect of casing treatment on the overall performance of the compressor decreases.

Table 3. Aerodynamic performance parameters of the compressors near-stall point.

Cases		Adiabatic Efficiency	Total Pressure Ratio
τ	SW	0.79511 (−)	1.9437 (−)
	G2	0.79696 (+0.23%)	1.9599 (+0.83%)
2τ	SW	0.82165 (−)	1.9116 (−)
	G2	0.82220 (+0.07%)	1.9228 (+0.59%)

The entropy contours of the blade tip plane at the near-stall condition are compared in Figure 9. It has been shown that the downward movement of the interface (between the TLF and incoming main flow) can be used to check the enhancement of flow stability [11,47]. Generally, the interface is regarded as the high gradient region of entropy contour, which is plotted with a black dashed line in Figure 11. Souleimani et al. [48] also stated that spike stall inception occurs when the interface reaches the blade tip leading edge plane. If not (i.e., the interface is still inside the blade passage), modal stall inception can be inferred. Therefore, these two criteria will be used in the following analysis as well.

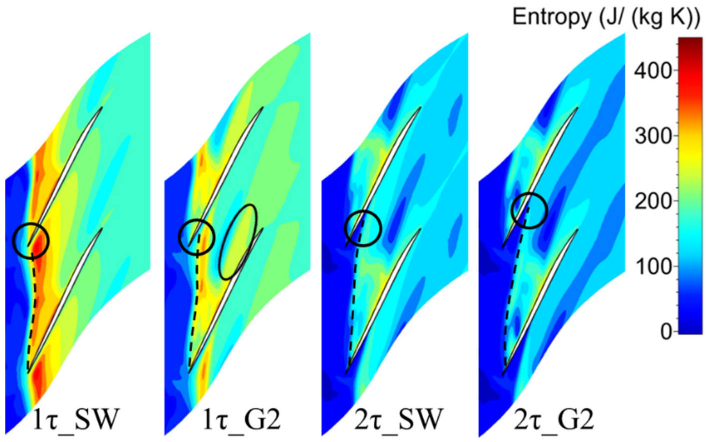

Figure 11. Entropy contours on the blade tip plane.

For the TCS of τ, the interface of the SW case is just located at the blade leading edge plane, which indicates that the spike stall inception may occur with further mass-flow rate reduced. After the use of CT, the interface is shifted to the downstream of the blade leading edge plane obviously, which means that the safe operating range is improved. From the change of entropy contour in G2, the loss generation near the blade leading edge is reduced obviously due to the improvement of TLF with the help of casing groove. However, the loss generation is increased on the blade suction surface near the trailing edge indicated by black oval, which means that the tip flow structure may be changed after the use of CT at the TCS of τ.

As the TCS is increased to 2τ, it can be observed that the interface of the SW case still stays inside the blade passage, from which we can infer that the modal stall inception may happen at a lower mass-flow rate. The interface is also shifted further downstream for the CT, which indicates that the flow stability is also enhanced with the help of casing groove. The slight reduction of entropy shows that the impact of TLF is decreased, and the flow field is improved to some extent. The reduction of loss generation in the region of blade tip after the use of CT at both TCS schemes is consistent with the improvement of compressor performance at the near-stall condition for the CTs shown in Figure 8.

Figure 12 depicts the relative Mach number contours in the blade tip region. The shock wave position is also marked with black line in the figure. For the SW case at the TCS of τ, a low energy fluid region (in the rectangle) on the pressure side exists close to the blade leading edge, due to the interaction between the TLF and shock wave. After the CT, the low energy fluid area is decreased significantly, which corresponds to the reduction of loss generation near the blade leading edge shown in Figure 11. For this reason, the tip-flow blockage is reduced and the flow capacity near the tip region is improved, which is beneficial to the SMI. In addition, the shock wave is shifted downstream obviously and its intensity becomes stronger, which can be seen from the higher Mach number before the sonic line near the blade suction side. As a result, the boundary layer on the blade suction surface is separated due to the stronger interaction between the shock wave and low energy boundary layer, which is consistent with the increase of loss generation on the blade suction surface near the trailing edge. Although the tip-flow blockage is increased to some extent due to the occurrence of the boundary layer separation, the flow capacity is improved because of the disappearance of the low energy fluid region. However, Figure 12 shows that there is no obvious change of tip flow structure after the CT at the TCS of 2τ.

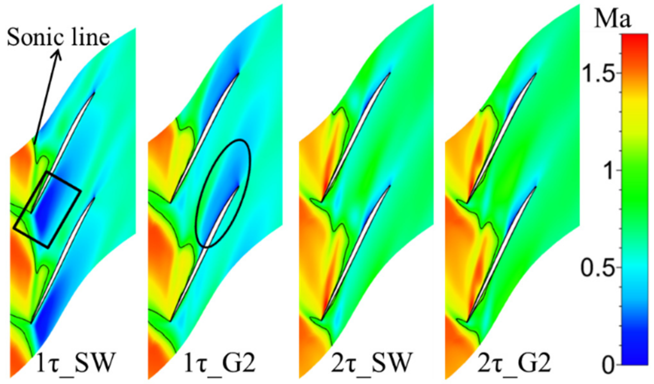

Figure 12. Relative Mach number contours on the blade tip plane.

The limiting streamlines on the blade suction surface are shown in Figure 13. The CT has remarkable influence on the tip flow structure at the TCS of τ, while there is no obvious change in terms of tip flow structure at the TCS of 2τ after CT. For the TCS of τ, there is no separation line near the blade tip due to the interaction between the shock wave and end wall boundary layer in the SW case. However, after CT, the separated boundary layer induced by the stronger shock wave tends to migrate toward the blade tip under the centrifugal force. Figure 14 shows the radial velocity contours on the mid-chord cross plane (indicated as Figure 11) at the TCS of τ. The radial velocity near the blade tip marked by black oval is increased remarkably after the CT. For this reason, additional mixing loss may occur caused by the interaction between the TLF and the climbing boundary layer separation. Therefore, for a better application of CT, the blade tip profile should be modified by using optimization method to adjust the shock position and strength during the design of CT.

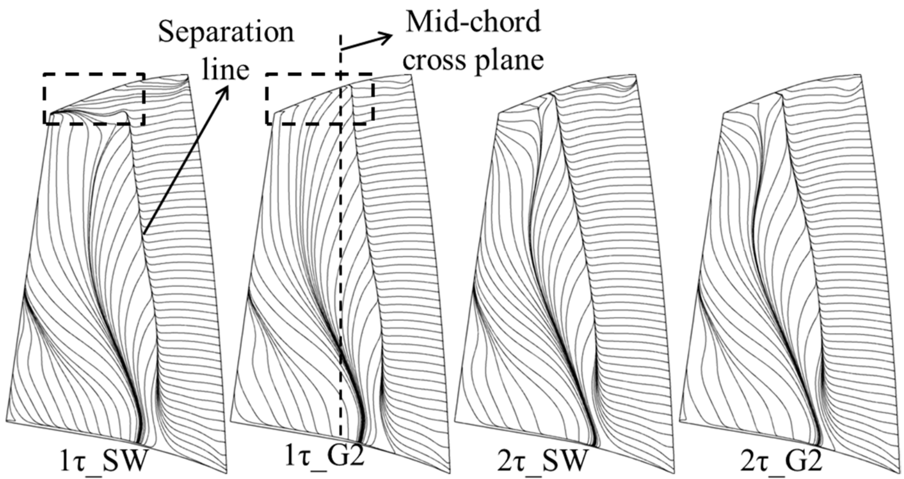

Figure 13. Limiting streamlines on the blade suction surface.

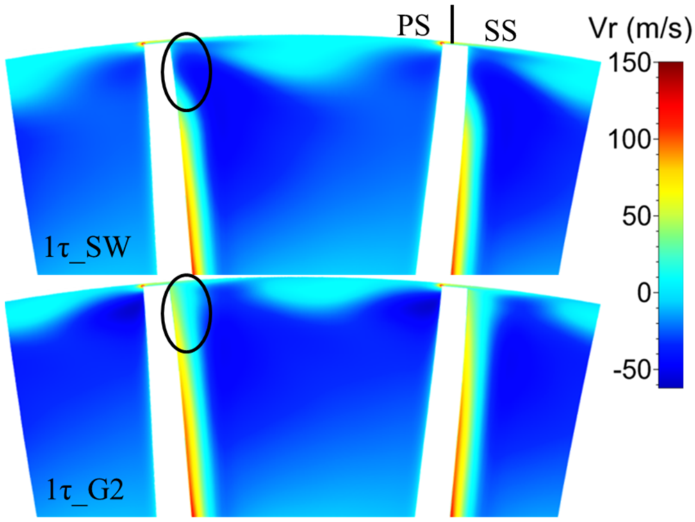

Figure 14. Radial velocity contours on the mid-chord cross plane at the TCS of τ.

Rabe and Hah [49] indicated that casing grooves increase the stall margin by reducing the flow incidence angle in a transonic compressor. It is also widely accepted that the flow incidence angle becomes larger and larger as the mass-flow rate is decreased gradually. Therefore, the reduction of incoming flow incidence angle may help to enhance the flow stability. The spanwise distribution of pitch-averaged relative flow angle at the rotor inlet plane is plotted in Figure 15. It should be mentioned that the variation trend of the flow incidence angle is the same as the change of the relative inlet flow angle considering the unchanged blade stagger angle. For the TCS of τ, the incidence angle near the blade tip is reduced slightly (about 1 degree) after CT, which agrees with the increase of tip flow capacity due to the reduction of flow blockage. However, there is almost no change of incidence angle after CT at the TCS of 2τ. Therefore, it seems that the reduction of flow incidence angle is not necessary to improve the flow stability for the transonic rotor in this paper.

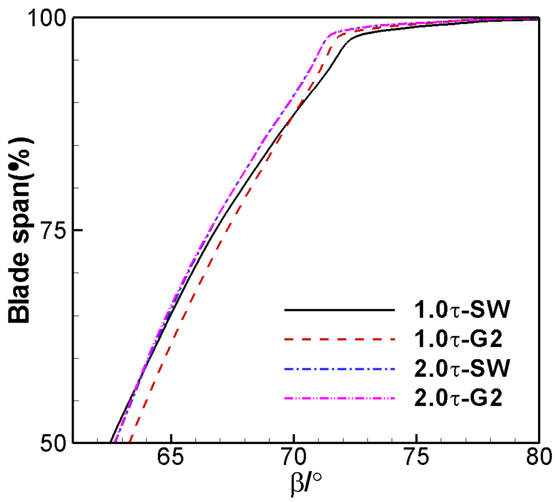

Figure 15. Spanwise distribution of pitch-averaged relative flow angle at the rotor inlet plane.

In public research, the difference of flow angle between exit and core aera at tip clearance can measure the intensity of local TLF, and the double leakage flow phenomenon (tip gap fluids that pass through the adjacent blade tip clearance) occurs more easily if the angle value is higher [35]. Khalid et al. also showed that double leakage flow contributes a lot to flow blockage and loss generation [3]. Thus, the tip-leakage flow angle (TLA), defined as the deviation of TLF exit direction from axial direction, is utilized to investigate the strength change of the local TLF and double leakage flow here.

The distributions of TLA at mid-gap for the SW case and CT schemes are presented in Figure 16. Compared with the SW case, the tip-leakage flow angle in both TCS schemes is reduced evidently along almost the whole blade chord range after CT, especially within the front part of the blade except for the location near the blade leading edge. The reduction of tip leakage angle is more obvious under the groove position and within a certain blade chord range just behind the groove, especially for the TCS of τ. Therefore, the intensity of local TLF is mitigated after the CT for both TCS schemes and the risk to cause the double leakage flow is also decreased, which is beneficial to enhance the flow stability and compressor performance at the near-stall point. Additionally, unlike the TCS of τ, there is no change of tip leakage angle near the blade leading edge at the TCS of 2τ after the CT of G2, which is in agreement with the unchanged incoming flow incidence angle shown in Figure 15.

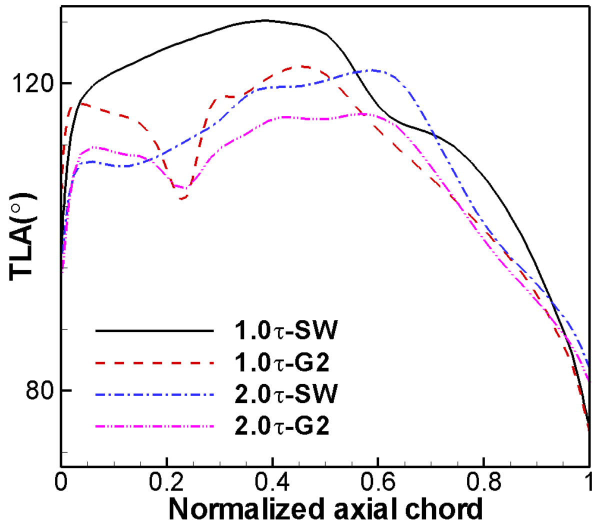

Figure 16. Distributions of tip-leakage flow angle at mid-gap.

In general, the strength of TLF is estimated by the value of the absolute vorticity. The normalized absolute vorticity is defined as:

$$\xi_n = \frac{|\xi|}{2\omega} \quad (2)$$

where $|\xi|$ and ω indicate the magnitude of absolute vorticity vector and angular velocity of the rotor respectively. The meridional contours of normalized absolute vorticity together with streamline distribution are shown in Figure 17, in which the vertical red dashed lines represent the axial location of the vortex core in the SW case at the two TCS schemes.

For the TCS of τ, compared with the SW case, both the peak value and the high vorticity area are reduced after the CT, which reveals that the intensity of TLF is mitigated and the tip-flow field is improved with the help of groove. In addition, the original vortex is separated into two parts and the vortex core of the new larger vortex is shifted downstream, which means that the tip flow structure has changed after the CT. For the TCS of 2τ, both the peak value and the high vorticity area are also decreased after CT. Therefore, the tip-flow field at the TCS of 2τ is also improved by the CT. However, there is no obvious variation of tip flow structure and only the vortex core is shifted downstream slightly. Overall, these results are consistent with the analysis above.

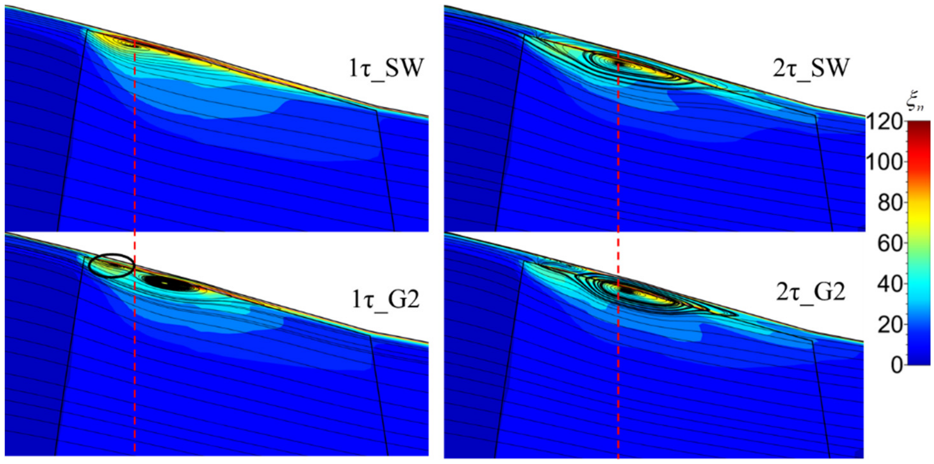

Figure 17. Pitch-averaged normalized absolute vorticity contours on the meridional plane.

Figure 18 compares the entropy contours on the mid-chord cross plane. At the TCS of τ, due to the upward migration of boundary layer separation induced by the shock wave interaction, the loss generation in black oval increases after CT compared with the SW case. However, both the peak value and high entropy area caused by the TLV are reduced remarkably, which is consistent with the improvement of the tip-flow field after CT. For the TCS of 2τ, compared with the SW case, the high entropy region and the peak value due to the impact of TLV are also decreased after CT, which corresponds to the reduction of TLF intensity.

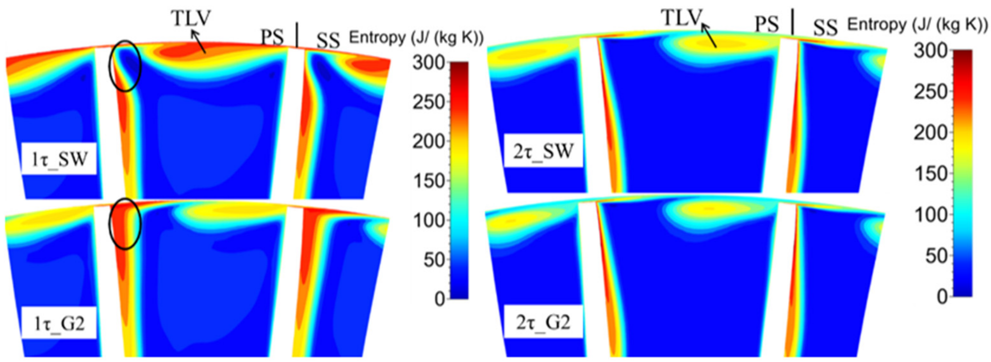

Figure 18. Entropy contours on the mid-chord cross plane.

In the stall inception process, the TLF of the transonic rotor can be divided into different parts along the chordwise, each of which plays a different role [50]. To gain a better insight into the effect of CT on the tip flow behaviors in this transonic rotor, the three-dimensional flow streamlines that start from tip gap over two important blade chord ranges are used to analyze the CT effect according to the flow features, i.e., LE-20% tip axial chord (denoted as the front part), 20–70% tip axial chord (denoted as the middle part). The front part TLF mainly governs the position of the interface near the blade suction surface, while the middle part TLF determines the interaction positions with the incoming flow near the pressure side of the adjacent blade and pushes the interface upstream.

The three-dimensional flow streamlines colored with relative Mach number over the blade LE to 20% tip axial chord at the TCS of τ are shown as Figure 19. In the SW case, a breakdown of TLV occurs due to the TLV/shock wave interaction between the TLV and shock wave. As a result, a large low-speed flow region is present and a severe flow blockage occurs near the adjacent blade pressure side, which leads to a remarkable local loss generation. Then, a portion of the front part TLF reaches to the neighboring blade tip and the phenomenon of double leakage occurs. The other portion of the front part TLF flows out of the passage directly. After the CT, the TLV breakdown disappears and the tip-flow field is modified significantly because of the reduction of the flow blockage by the low-speed flow. Moreover, the double leakage phenomenon is alleviated slightly.

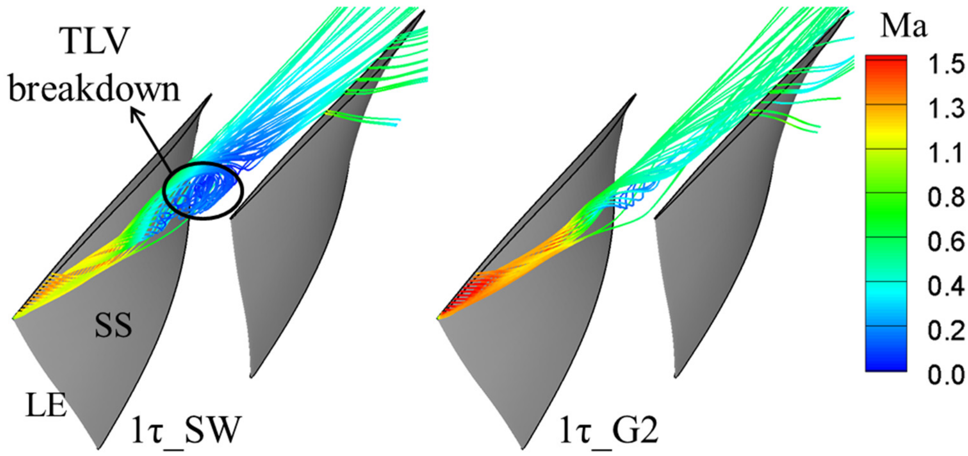

Figure 19. Volume streamlines released from the blade LE-20% tip axial chord at the TCS of τ.

As shown in Figure 20, the streamlines in Figure 19 are re-colored with normalized helicity (H_n), which has been used to study the TLV breakdown phenomenon by Furukawa et al. [8]; it can be defined as the equation below:

$$H_n = \frac{\xi \cdot w}{|\xi||w|} \tag{3}$$

where ξ and w denote absolute vorticity vectors and the relative flow velocity vectors respectively. It is worth noting that in the vortex core, the magnitude of the normalized helicity tends to ± 1, and its sign represents the vortex swirl direction relative to the relative velocity.

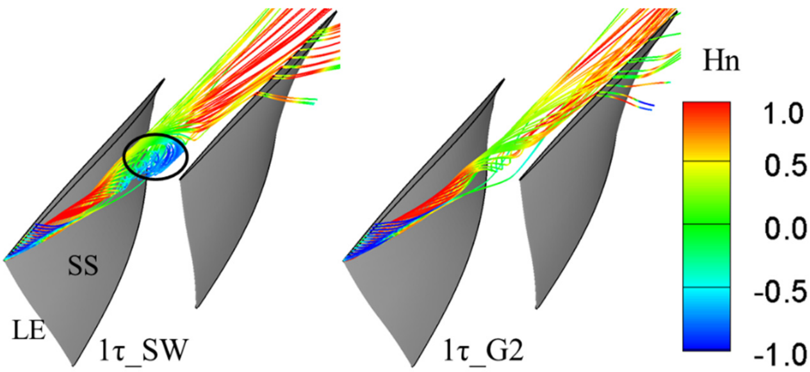

Figure 20. Volume streamlines released from the blade LE-20% tip axial chord colored with normalized helicity at the TCS of τ.

It can be observed that the normalized helicity marked by the black oval downstream of the shock wave changes drastically. The swirl direction of the TLV changes rapidly, which causes the occurrence of the TLV breakdown. The normalized helicity becomes positive again downstream of the TLV breakdown area. After the CT, there is no drastic change of the sign of H_n after the interaction of shock wave. Therefore, the disappearance of the TLV breakdown contributes to the tip-flow field. It has been found that the flow blockage resulting from the TLV breakdown deeply affects the compressor stall inception [8,51]. The disappearance of the vortex breakdown was also observed by Sakuma et al. [28] after the application of circumferential grooved CT. Therefore, at the TCS of τ, the compressor flow stability can be attenuated by the suppression of the TLV breakdown due to the interaction between shock wave and the front part TLF. In this way, the tip-flow blockage is reduced and the likelihood of occurrence of interface spillage is decreased, which is beneficial to the SMI.

Figure 21 shows the three-dimensional flow streamlines released from the 20% to 70% tip axial chord at the TCS of τ. For the SW case, a large portion of the middle part TLF hits the pressure side within the front part chord range of the adjacent blade and organizes the double leakage. Near the pressure side of the adjacent blade, the interface has already arrived at the blade leading plane and the interface spillage will occur for a slightly lower mass-flow rate. After CT, the double leakage phenomenon is almost removed near the leading edge of the rotor blade, and the risk of interface spillage is reduced, which corresponds to the downward movement of the interface.

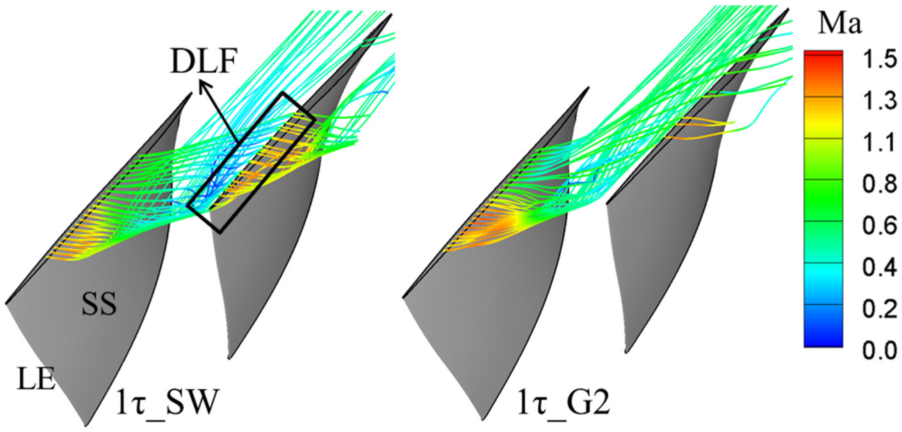

Figure 21. Volume streamlines released from the 20–70% tip axial chord at the TCS of τ.

The TLF streamlines released from the blade LE-70% tip axial chord at the TCS of 2τ are shown in Figure 22. Compared with the TCS of τ, one can observe that the TLV breakdown does not occur after the interference between the front part TLF and shock wave in the SW case. Additionally, there are also no double leakage flows, and the interface is still located behind the blade leading edge. After CT, the TLF is further away from the adjacent blade pressure surface near the leading edge, which means that the interface position is shifted more downstream due to the groove effect. In addition, within the rear half blade chord range, the double leakage phenomenon is relieved to some extent. Therefore, the strength of TLF is decreased, which is helpful for the SMI.

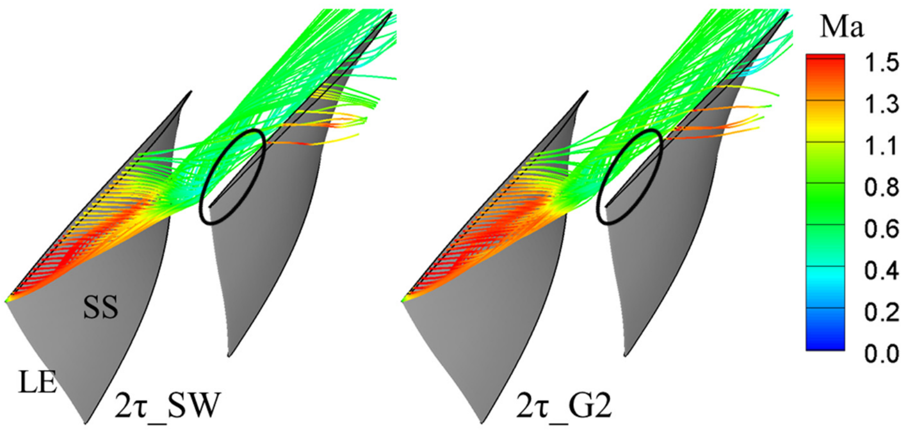

Figure 22. Three-dimensional flow streamlines released from the blade LE-70% tip axial chord at the TCS of 2τ.

From the analysis above, the tip flow structure is changed after the CT of G2 at the TCS of τ. The effects of casing groove on TLF are different for the different part TLF. For the front part TLF, the TLV breakdown phenomenon disappears and the tip blockage is decreased obviously, which reduces the risk of interface spillage at the blade leading edge. However, the double leakage phenomenon is almost removed due to the impact of groove on the middle part TLF. The improvement of both the two different parts TLF corresponds to the TLF intensity reduction after the use of CT, which contributes to the flow stability enhancement. At the TCS of 2τ, the flow structure after CT of G2 is not changed obviously and only the interface position is shifted more downstream with the help of the groove. Figure 11 shows that there are different stall inception processes for the TCS schemes of τ and 2τ. Therefore, according to the change of tip flow structure, it can be concluded that the control mechanisms of CT may be different for different TCS schemes due to the distinction of stall inception process, which will be investigated by performing more accurate and advanced unsteady simulations.

5. Conclusions

In this paper, in a transonic axial flow compressor rotor, the effect of circumferential single-grooved CT on the tip-flow stability and corresponding control mechanism under tip-clearance effect is investigated numerically. The conclusions are summarized as follows:

(1) A parametric study indicates that the CT schemes are most effective at the TCS of 1.5τ. The flow stability can be improved efficiently when the grooves are located from 10% to 40% of the blade tip axial chord, and G2 is the best CT scheme for all the three TCS schemes in terms of the SMI.
(2) The interface location is shifted downwards after the effective CTs. The TLF intensity, the flow loss and tip-flow blockage are all decreased to a different extent, which leads to stability enhancement. The quantitative analysis of the relative inlet flow angle shows that the reduction of flow incidence angle is not necessary to enhance the flow stability for the transonic rotor in this paper.
(3) The control mechanisms of CT may be different for different TCS schemes due to the distinction of the process of the stall inception. For a better application of CT, the blade tip profile should be modified by using an optimization method to adjust the shock position and strength during the design of more efficient CT. In this way, the impact of new negative tip flow phenomenon (e.g., boundary-layer separation induced by the stronger shock wave) can be relieved after the application of a casing groove.

Author Contributions: Conceptualization, X.W. and X.M.; Data curation, X.W. and B.Z.; Formal analysis, X.W. and X.M.; Funding acquisition, X.M. and B.L.; Investigation, X.W. and B.Z.; Methodology, X.M.; Supervision, B.L.; Writing—original draft, X.W.; Writing—review and editing, X.M. and B.Z. All authors have read and agreed to the published version of the manuscript.

Funding: This paper is supported by the National Natural Science Foundation of China under Grant 52106057 and 51790512, the National Science and Technology Major Project under Grant 2017-II-0001–0013, the Foundation of State Level Key Laboratory of Airfoil and Cascade Aerodynamics under Grant 614220120050; these supports are gratefully acknowledged.

Conflicts of Interest: The authors declare no conflict of interest.

Nomenclature

Symbols		Abbreviations	
β	relative flow angle	AR	aspect ratio
H_n	normalized helicity	CT	casing treatment
m	mass-flow rate	LE	leading edge
w	relative flow velocity	NDP	near-design point
π	total pressure ratio	NSP	near-stall point
τ	design tip clearance	PS	pressure surface
ξ	absolute vorticity vector	SMI	stall-margin improvement
ξ_n	normalized absolute vorticity	SS	suction surface
		SW	smooth wall
		TCS	tip-clearance size
		TE	trailing edge
		TLA	tip-leakage flow angle
		TLF	tip-leakage flow
		TLV	tip-leakage vortex

References

1. Koch, C.C.; Smith, L.H. Loss sources and magnitudes in axial-flow compressors. *J. Eng. Power* **1976**, *98*, 411–424. [CrossRef]
2. Suder, K.L. Blockage Development in a Transonic, Axial Compressor Rotor. *J. Turbomach.* **1998**, *120*, 465–476. [CrossRef]
3. Khalid, S.A.; Khalsa, A.S.; Waitz, I.A.; Tan, C.S.; Greitzer, E.M.; Cumpsty, N.A.; Adamczyk, J.J.; Marble, F.E. Endwall Blockage in Axial Compressors. *J. Turbomach.* **1999**, *121*, 499–509. [CrossRef]
4. Gourdain, N.; Wlassow, F.; Ottavy, X. Effect of Tip Clearance Dimensions and Control of Unsteady Flows in a Multi-Stage High-Pressure Compressor. *J. Turbomach.* **2012**, *134*, 051005. [CrossRef]
5. Sakulkaew, S.; Tan, C.S.; Donahoo, E.; Cornelius, C.; Montgomery, M. Compressor Efficiency Variation With Rotor Tip Gap From Vanishing to Large Clearance. *J. Turbomach.* **2013**, *135*, 031030. [CrossRef]
6. Han, L.; Yuan, W.; Wang, Y. Influence of tip leakage flow and ejection on stall mechanism in a transonic tandem rotor. *Aerosp. Sci. Technol.* **2018**, *77*, 499–509. [CrossRef]
7. Wang, Z.; Lu, B.; Liu, J.; Hu, J. Numerical simulation of unsteady tip clearance flow in a transonic compressor rotor. *Aerosp. Sci. Technol.* **2018**, *72*, 193–203. [CrossRef]
8. Furukawa, M.; Inoue, M.; Saiki, K.; Yamada, K. The Role of Tip Leakage Vortex Breakdown in Compressor Rotor Aerodynamics. *J. Turbomach.* **1999**, *121*, 469–480. [CrossRef]
9. Yamada, K.; Funazaki, K.; Sasaki, H. Numerical Investigation of Relation Between Unsteady Behavior of Tip Leakage Vortex and Rotating Disturbance in a Transonic Axial Compressor Rotor. In Proceedings of the ASME Turbo Expo 2008: Power for Land, Sea and Air, Berlin, Germany, 9–13 June 2008.
10. Deng, X.; Zhang, H.; Chen, J.; Sasaki, H. Unsteady Tip Clearance Flow in a Low-Speed Axial Compressor Rotor with Upstream and Downstream Stators. In Proceedings of the ASME Turbo Expo 2005: Power for Land, Sea and Air, Reno, NV, USA, 6–9 June 2005.
11. Cameron, J.D.; Bennington, M.A.; Ross, M.H.; Morris, S.C.; Du, J.; Lin, F.; Chen, J. The Influence of Tip Clearance Momentum Flux on Stall Inception in a High-Speed Axial Compressor. *J. Turbomach.* **2013**, *135*, 051005. [CrossRef]
12. Zhang, B.; Mao, X.; Wu, X.; Liu, B. Effects of Tip Leakage Flow on the Aerodynamic Performance and Stability of an Axial-Flow Transonic Compressor Stage. *Energies* **2021**, *14*, 4168. [CrossRef]
13. Grondin, J.; Trébinjac, I.; Rochuon, N. Rotating Instabilities Versus Rotating Stall in a High-Speed Centrifugal Compressor. In Proceedings of the ASME Turbo Expo 2018: Turbomachinery Technical Conference and Exposition, Oslo, Norway, 11–15 June 2018. GT2018-76916.
14. Trébinjac, I.; Benichou, E.; Buffaz, N. Full-annulus simulation of the surge inception in a transonic centrifugal compressor. *J. Therm. Sci.* **2015**, *24*, 442–451. [CrossRef]
15. Cravero, C.; Marsano, D. Criteria for the Stability Limit Prediction of High Speed Centrifugal Compressors With Vaneless Diffuser: Part I—Flow Structure Analysis. In Proceedings of the ASME Turbo Expo 2020: Turbomachinery Technical Conference and Exposition, London, UK, 22–26 June 2020.
16. Cravero, C.; Marsano, D. Criteria for the Stability Limit Prediction of High Speed Centrifugal Compressors With Vaneless Diffuser: Part II—The Development of Prediction Criteria. In Proceedings of the ASME Turbo Expo 2020: Turbomachinery Technical Conference and Exposition, London, UK, 22–26 June 2020.
17. Hathaway, M.D. Passive Endwall Treatments for Enhancing Stability. U.S. Patent NASA TM-214409, 1 July 2007.
18. Fujita, H.; Takata, H. A study on configurations of casing treatment for axial flow compressors. *Bull. JSME* **1984**, *27*, 1675–1681. [CrossRef]
19. Shabbir, A.; Adamczyk, J.J. Flow mechanism for stall margin improvement due to circumferential casing grooves on axial compressors. *J. Turbomach.* **2005**, *127*, 708–717. [CrossRef]

20. Chen, H.; Huang, X.; Shi, K.; Song, F.; Ross, M.; Bennington, M.A.; Cameron, J.D.; Morris, S.C.; Mcnulty, S.; Wadia, A. A computational fluid dynamics study of circumferential groove casing treatment in a transonic axial compressor. *J. Turbomach.* **2014**, *136*, 031003. [CrossRef]
21. Mao, X.; Liu, B.; Zhao, H. Numerical analysis of the circumferential grooves casing treatment in a counter-rotating axial flow compressor. *Appl. Therm. Eng.* **2018**, *130*, 29–39. [CrossRef]
22. Bailey, E.E. Effect of Grooved Casing Treatment on the Flow Range Capability of a Single-Stage Axial-Flow Compressor. U.S. Patent NASA TM2459, 1 January 1972.
23. Houghton, T.; Day, I. Enhancing the Stability of Subsonic Compressors Using Casing Grooves. *J. Turbomach.* **2011**, *133*, 021007. [CrossRef]
24. Houghton, T.; Day, I. Stability enhancement by casing grooves: The importance of stall inception mechanism and solidity. *J. Turbomach.* **2012**, *134*, 021003. [CrossRef]
25. Juan, D.; Jichao, L.; Lipeng, G.; Feng, L.; Jingyi, C. The Impact of Casing Groove Location on Stall Margin and Tip Clearance Flow in a Low-Speed Axial Compressor. *J. Turbomach.* **2016**, *138*, 121007. [CrossRef]
26. Liu, L.; Li, J.; Nan, X.; Lin, F. The stall inceptions in an axial compressor with single circumferential groove casing treatment at different axial locations. *Aerosp. Sci. Technol.* **2016**, *59*, 145–154. [CrossRef]
27. Mao, X.; Liu, B.; Tang, T.; Zhao, H. The impact of casing groove location on the flow instability in a counter-rotating axial flow compressor. *Aerosp. Sci. Technol.* **2018**, *76*, 250–259. [CrossRef]
28. Sakuma, Y.; Watanabe, T.; Himeno, T.; Kato, D.; Murooka, T.; Shuto, Y. Numerical Analysis of Flow in a Transonic Compressor With a Single Circumferential Casing Groove: Influence of Groove Location and Depth on Flow Instability. *J. Turbomach.* **2014**, *136*, 031017. [CrossRef]
29. Sakuma, Y.; Watanabe, T.; Himeno, T.; Kato, D.; Murooka, T.; Shuto, Y. Numerical analysis of flow in a transonic compressor with a single circumferential casing groove: Application to two different compressor rotors. In Proceedings of the ASME Turbo Expo 2014: Turbine Technical Conference & Exposition, Düsseldorf, Germany, 16–20 June 2014. GT2014-26691.
30. Mirzabozorg, M.A.S.; Bazazzadeh, M.; Hamzezade, M. Numerical study on the effect of single shallow circumferential groove casing treatment on the flow field and the stability of a transonic compressor. *J. Appl. Fluid Mech.* **2017**, *10*, 257–265.
31. Takata, H.; Tsukuda, Y. Stall margin improvement by casing treatment-its mechanism and effectiveness. *J. Eng. Power* **1977**, *99*, 121–133. [CrossRef]
32. Rolfes, M.; Lange, M.; Vogeler, K. Experimental investigation of circumferential groove casing treatments for large tip clearances in a low speed axial research compressor. In Proceedings of the ASME Turbo Expo 2015: Turbine Technical Conference & Exposition, Montreal, QC, Canada, 15–19 June 2015. GT2015-42646.
33. Rolfes, M.; Lange, M.; Vogeler, K.; Mailach, R. Experimental and Numerical Investigation of a Circumferential Groove Casing Treatment in a Low-Speed Axial Research Compressor at Different Tip Clearances. *J. Turbomach.* **2017**, *139*, 121009. [CrossRef]
34. Hamzezade, M.; Agha Seyed Mirzabozorg, M.; Bazazzadeh, M. Numerical study of the effect of the tip gap size and using a single circumferential groove on the performance of a multistage compressor. *J. Comput. Appl. Mech.* **2019**, *50*, 54–62.
35. Beheshti, B.H.; Teixeira, J.A.; Ivey, P.C.; Ghorbanian, K.; Farhanieh, B. Parametric Study of Tip Clearance—Casing Treatment on Performance and Stability of a Transonic Axial Compressor. In Proceedings of the ASME Turbo Expo 2004: Power for Land, Sea, and Air, Vienna, Austria, 14–17 June 2004. GT2004-53390.
36. Cevik, M.; Duc Vo, H.; Yu, H. Casing Treatment for Desensitization of Compressor Performance and Stability to Tip Clearance. *J. Turbomach.* **2016**, *138*, 121008. [CrossRef]
37. Lonnie, R.; Royce, D.M. Performance of Single-Stage Axial-Flow Transonic Compressor with Rotor and Stator Aspect Ratios of 1.19 and 1.26, Respectively, and with Design Pressure Ratio of 1.82. U.S. Patent NASA-TP-1338, 1 November 1978.
38. Chen, J.; Hathaway, M.D.; Herrick, G.P. Prestall Behavior of a Transonic Axial Compressor Stage via Time-Accurate Numerical Simulation. *J. Turbomach.* **2008**, *130*, 041014. [CrossRef]
39. NUMECA International. *IGG v8.7, User Manual*; NUMECA International: Brussels, Belgium, 2009.
40. NUMECA International. *FINE/Turbo v8.7, User Manual*; NUMECA International: Brussels, Belgium, 2009.
41. Spalart, P.R.; Allmaras, S.R. A one-equation turbulence model for aerodynamic flows. In Proceedings of the 30th Aerospace Sciences Meeting and Exhibit, Reno, NV, USA, 6–9 January 1992. AIAA-92-0439.
42. Milidonis, K.; Semlitsch, B.; Hynes, T. Effect of Clocking on Compressor Noise Generation. *AIAA J.* **2018**, *56*, 4225–4231. [CrossRef]
43. Zhu, W.; Wang, S.; Zhang, L.; Ding, J.; Wang, Z. Effect of tip clearance size on the performance of a low-reaction transonic axial compressor rotor. *Proc. Inst. Mech. Eng. Part A J. Power Energy.* **2020**, *234*, 127–142. [CrossRef]
44. NUMECA International. *AutoGrid5 v8.7, User Manual*; NUMECA International: Brussels, Belgium, 2009.
45. Biollo, R.; Benini, E. Shock/boundary-layer/tip-clearance interaction in a transonic rotor blade. *J. Propuls. Power* **2009**, *25*, 668–677. [CrossRef]
46. Gao, L.; Li, X.; Feng, X.; Liu, B. The effect of tip clearance on the performance of contra-rotating compressor. In Proceedings of the ASME Turbo Expo 2012: Turbine Technical Conference and Exposition, Copenhagen, Denmark, 11–15 June 2012. GT2012-68801.
47. Vo, H.D.; Tan, C.S.; Greitzer, E.M. Criteria for Spike Initiated Rotating Stall. *J. Turbomach.* **2008**, *130*, 011023. [CrossRef]
48. Souleimani, Y.; Vo, H.D.; Yu, H. Performance desensitization for a high-speed axial compressor. In Proceedings of the ASME Turbo Expo 2018: Turbomachinery Technical Conference and Exposition, Oslo, Norway, 11–15 June 2018. GT2018-77203.

49. Rabe, D.C.; Hah, C. Application of Casing Circumferential Grooves for Improved Stall Margin in a Transonic Axial Compressor. In Proceedings of the ASME Turbo Expo 2002: Power for Land, Sea, and Air, Amsterdam, The Netherlands, 3–6 June 2002. GT2002-30641.
50. Du, J.; Lin, F.; Chen, J.; Nie, C.; Biela, C. Flow Structures in the Tip Region for a Transonic Compressor Rotor. *J. Turbomach.* **2013**, *135*, 031012. [CrossRef]
51. Schlechtriem, S.; Lötzerich, M. Breakdown of Tip Leakage Vortices in Compressors at Flow Conditions Close to Stall. In Proceedings of the ASME 1997 International Gas Turbine and Aeroengine Congress and Exhibition, Orlando, FL, USA, 2–5 June 1997. 97-GT-041.